ARTICLES
PUBLISHED ONLINE: 8 JULY 2012 | DOI: 10.1038/NMAT3371
nature materials

Ferroelectric order in individual nanometre-scale crystals

Mark J. Polking[1], Myung-Geun Han[2], Amin Yourdkhani[3,4], Valeri Petkov[5], Christian F. Kisielowski[6], Vyacheslav V. Volkov[2], Yimei Zhu[2], Gabriel Caruntu[3,4], A. Paul Alivisatos[7,8]* and Ramamoorthy Ramesh[1,7]*

Ferroelectricity in finite-dimensional systems continues to arouse interest, motivated by predictions of vortex polarization states and the utility of ferroelectric nanomaterials in memory devices, actuators and other applications. Critical to these areas of research are the nanoscale polarization structure and scaling limit of ferroelectric order, which are determined here in individual nanocrystals comprising a single ferroelectric domain. Maps of ferroelectric structural distortions obtained from aberration-corrected transmission electron microscopy, combined with holographic polarization imaging, indicate the persistence of a linearly ordered and monodomain polarization state at nanometre dimensions. Room-temperature polarization switching is demonstrated down to ~5 nm dimensions. Ferroelectric coherence is facilitated in part by control of particle morphology, which along with electrostatic boundary conditions is found to determine the spatial extent of cooperative ferroelectric distortions. This work points the way to multi-Tbit/in^2 memories and provides a glimpse of the structural and electrical manifestations of ferroelectricity down to its ultimate limits.

New synthetic strategies for nanostructures of functional materials and new nanoscale characterization tools have rapidly expanded knowledge of fundamental physical properties at finite dimensions over the past two decades. A recent acceleration of this trend has been fuelled in part by a transition from traditional ensemble measurements to single-particle studies, which reveal powerful new insights previously obscured by statistical averaging. Although much progress has been made in the understanding of nanoscale photophysical[1,2], magnetic[3] and many other functional properties, understanding of the basic physics of ferroelectric nanomaterials remains far less advanced, despite the immense practical potential of these materials in nonvolatile memory devices, high-performance dielectrics and many other applications[4,5]. The picture of nanoscale ferroelectricity has continued to evolve, from the earliest reports indicating complete suppression of ferroelectric behaviour[6,7] to more recent studies[8–10] demonstrating an enhancement of local ferroelectric distortions coincident with a decline in the overall polar distortion, and finally to theoretical work predicting toroidal polarization patterns[11,12]. Understanding of the physical mechanisms responsible for these profound changes in ferroelectric behaviour at finite dimensions is similarly unsettled, with literature reports implicating depolarization fields, internal strains, and other driving forces for the size-dependent decay of polar order[13–15]. Progress in understanding these questions has been hindered in part by the relative paucity of high-quality, monocrystalline ferroelectric nanomaterials[16–18] with well-defined sizes, shapes and surfaces, and by the reliance on ensemble-averaged measurement techniques, which obscure the local behaviour of individual crystals. Here, ferroelectric order is examined down to its ultimate scaling limit in individual, isolated nanocrystals of the semiconducting ferroelectric GeTe and the archetypal oxide ferroelectric $BaTiO_3$ consisting of a single ferroelectric domain. Examination of individual colloidally synthesized nanocrystals with regular shapes and atomically flat surfaces enables the intrinsic physics of ferroelectric order to be revealed free from substrate effects, statistical averaging, and artefacts induced by processing damage, providing for the first time a detailed glimpse of the local structural and electrical behaviour of ferroelectric nanomaterials at the smallest accessible length scales. Aberration-corrected transmission electron microscopy (TEM) is employed to map local ferroelectric distortion patterns at the unit-cell scale with picometre-level precision. These detailed TEM studies are complimented with off-axis electron holography studies of individual $BaTiO_3$ nanocubes that enable direct imaging of the ferroelectric polarization. We find that a monodomain ferroelectric state with an overall, linearly ordered polarization remains stable in these nanocrystals down to sub-10 nm dimensions, albeit with significant degradation of the structural coherence revealed by ensemble-averaged atomic pair distribution function (PDF) studies. Direct electrical measurements of individual $BaTiO_3$ nanocrystals demonstrate room-temperature polarization switching of sub-10 nm nanocubes and reveal the disappearance of ferroelectric behaviour below a critical size of 5–10 nm, indicating the ultimate limit for the size-scaling of the polar phase. Comparisons between highly conducting GeTe and insulating $BaTiO_3$ nanocrystals and between $BaTiO_3$ nanocrystals with different sizes and morphologies enable the influences of

[1]Department of Materials Science and Engineering, University of California, Berkeley, Berkeley, California 94720, USA, [2]Condensed Matter Physics and Materials Sciences Department, Brookhaven National Laboratory, Upton, New York 11973, USA, [3]Department of Chemistry, University of New Orleans, New Orleans, Louisiana 70148, USA, [4]Advanced Materials Research Institute, University of New Orleans, New Orleans, Louisiana 70148, USA, [5]Department of Physics, Central Michigan University, Mount Pleasant, Michigan 48859, USA, [6]National Center for Electron Microscopy, Lawrence Berkeley National Laboratory, Berkeley, California 94720, USA, [7]Materials Sciences Division, Lawrence Berkeley National Laboratory, Berkeley, California 94720, USA, [8]Department of Chemistry, University of California, Berkeley, Berkeley, California 94720, USA. *e-mail: APAlivisatos@lbl.gov; rramesh@berkeley.edu.

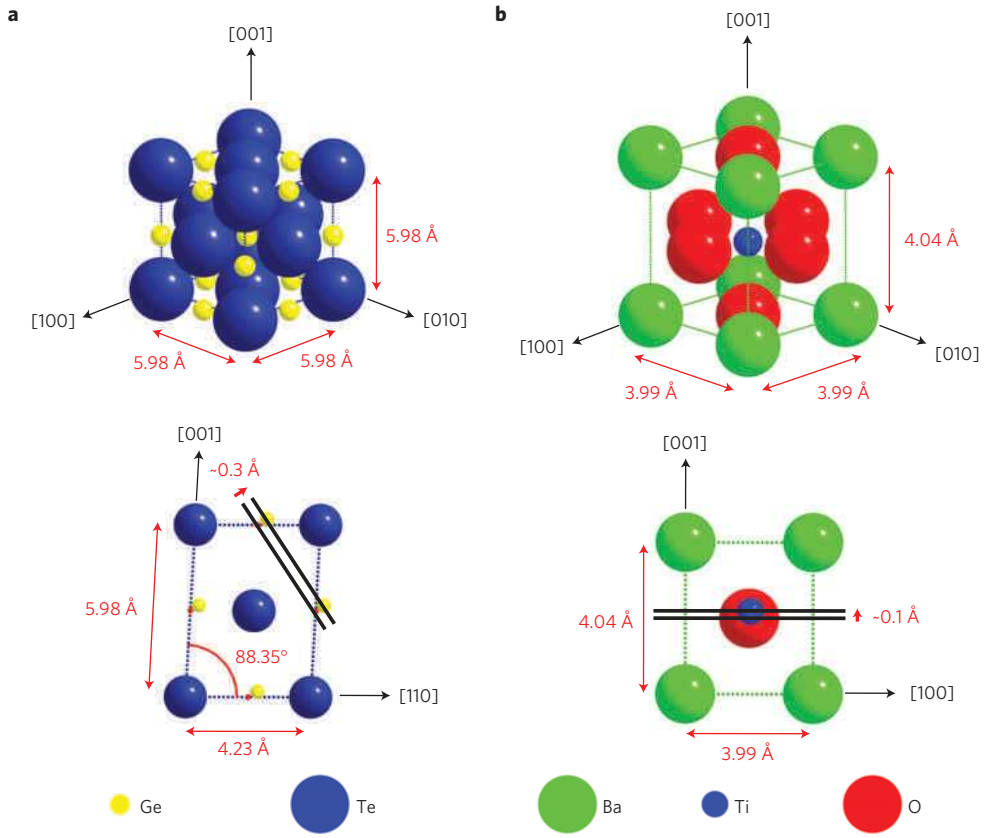

Figure 1 | Ferroelectric distortions of the GeTe and $BaTiO_3$ conventional unit cells. a, Conventional unit cell of GeTe in the rhombohedral phase; a [110]-type projection used for atomic-resolution TEM is shown. The rhombohedral distortion of the unit cell results in an angular distortion of the principal axes accompanied by a relative displacement of the Ge sublattice with respect to the Te sublattice (small red arrows). **b**, Conventional unit cell of tetragonal $BaTiO_3$; a [100]-type projection used for atomic-resolution TEM imaging is shown. The ferroelectric phase transition results in a tetragonal distortion of the unit cell along a [001]-type axis and a displacement of the titanium cation from the centre of the unit cell, removing the inversion symmetry. Structural data are taken from refs 25 and 30. The small red dots denote the positions of the Ge cations before the sublattice shift; the black bars and corresponding small red arrows indicate the magnitude and direction, respectively, of the sublattice displacements.

the depolarizing field and surface structure to be independently examined, providing a means of identifying the fundamental factors governing the nature of the polar state at finite dimensions. The results described here provide an atomic-scale picture of local polarization structure and enable new nanoscale devices based on individual, isolated ferroelectric domains.

Germanium telluride (GeTe), a narrow-gap semiconductor, is the simplest material to undergo a ferroelectric phase transition, with one anion and one cation per primitive unit cell[19–21]. Below its Curie temperature of ~625 K, GeTe spontaneously transforms from the rock salt structure to a polar rhombohedral structure with an angular distortion of ~1.65° between the principal axes and a relative displacement of the Ge and Te sublattices along a [111] direction (Fig. 1a; ref. 22). GeTe exists naturally in a non-stoichiometric phase with a high density of Ge vacancies, leading to a density of free holes often exceeding 10^{21} cm^{-3} (refs 21,23). Although this high free carrier density inhibits practical switching of the spontaneous polarization, GeTe undergoes a spontaneous polar ordering transition like the better-known perovskite ferroelectrics and is thus regarded as a ferroelectric in a broader sense[24]. Despite its practical limitations as a ferroelectric, GeTe presents an interesting test case of a ferroelectric metal with strong internal screening of the spontaneous polarization and minimal depolarization effects. The classic perovskite ferroelectric $BaTiO_3$, in contrast, is an insulating oxide with a Curie temperature of around 400 K (ref. 25). Below this temperature, the cubic prototype phase undergoes a tetragonal distortion along a [001]-type axis with a corresponding displacement of the central Ti cation along the same direction (Fig. 1b), producing a spontaneous polarization[25].

Monocrystalline nanoparticles of both materials were prepared using colloidal synthetic techniques. GeTe nanocrystals with an average diameter of 8 nm (Supplementary Fig. S1) were prepared through reaction of Ge(II) bis-bis(trimethylsilyl)amide and trioctylphosphine-tellurium in the presence of a 1-dodecanethiol surfactant, as described in a previous paper[18]. Nanocubes of $BaTiO_3$ with average side lengths of 8, 10, and 15 nm (Supplementary Fig. S1) were prepared using a two-phase aqueous/organic synthesis procedure in a pressure vessel, following a previous literature report[17], and quasi-spherical particles with an average diameter of 10 nm (Supplementary Fig. S1) were prepared using a modification of this procedure in which the polarity of the reaction medium was decreased through addition of a supplementary volume of decanol in the mixture formed by water, ethanol and decanol, respectively.

Ferroelectric order arises from a spontaneous distortion of the crystal lattice, leading to relative displacements of the ionic sublattices, generally on the order of 0.05–0.4 Å (refs 24,26,27). Direct, atomic-resolution imaging of these displacements provides a powerful means of analysing local polarization patterns[26,27]. Nanocrystals of GeTe, with an average diameter of 8 nm, and nanocubes of $BaTiO_3$, with an average size of 15 nm, were imaged under negative C_s imaging conditions using the aberration-corrected TEAM 1 microscope, a modified FEI Titan 80-300 with an information limit of ~0.5 Å. Through-focus series of high-resolution TEM images of GeTe nanocrystals in [110]

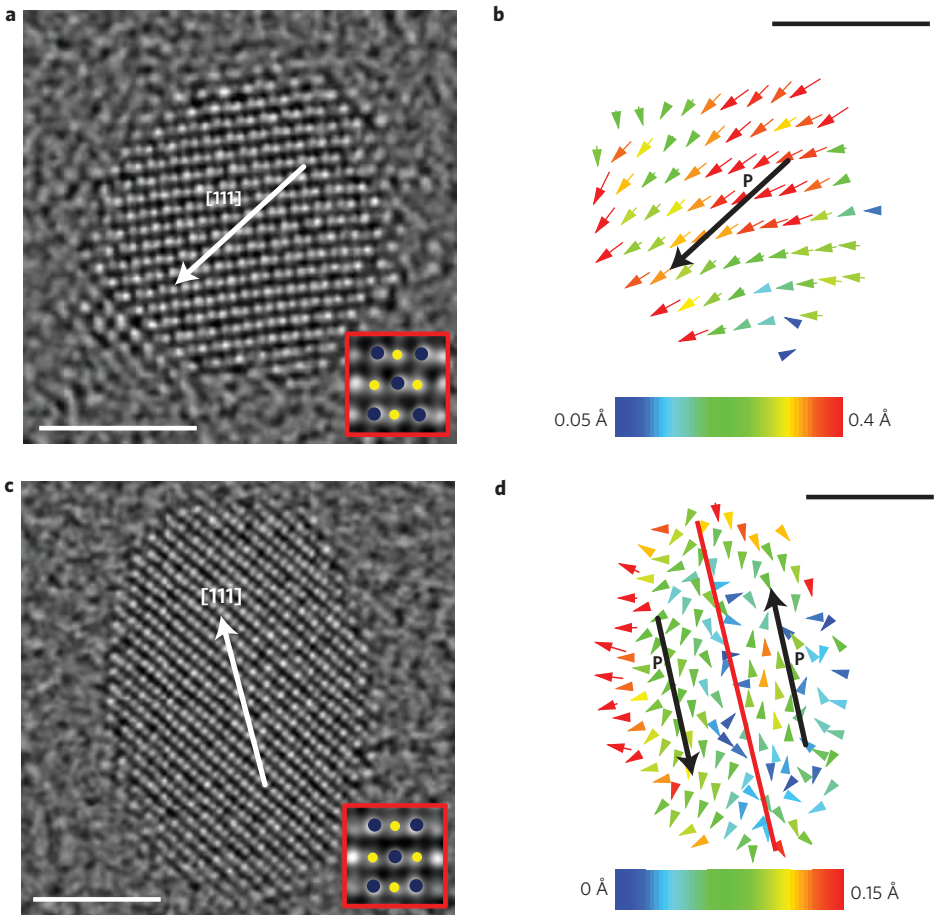

Figure 2 | Atomic-resolution reconstructed phase images and polar displacement maps of individual GeTe monocrystalline nanoparticles. **a**,**b**, Reconstructed phase image of a GeTe nanocrystal (**a**) and corresponding polar displacement map (**b**) illustrating a nearly linear, coherent displacement pattern along a [111] axis. Inset: magnified view of a GeTe unit cell from the particle demonstrating resolution of Ge (yellow) and Te (blue) columns (scale bars in **a** and **b** are 3 nm, vector magnitudes are given by the colour scale). **c**,**d**, Reconstructed phase image of a GeTe nanocrystal (**c**) and corresponding polar displacement map (**d**) illustrating an inversion domain boundary. Inset: magnified view of a GeTe unit cell from the particle demonstrating resolution of Ge and Te columns (scale bars in **c** and **d** are 3 nm, vector magnitudes are given by the colour scale). All images were taken along a [110]-type projection.

orientations and $BaTiO_3$ nanocrystals in [100]-type orientations were reconstructed using the Gerchberg–Saxton algorithm to recover the phase of the electron wavefunction at the exit plane of the specimen, which contains directly interpretable information about the atomic structure down to the information limit of the microscope[28,29]. Unit cell-scale maps of the local ferroelectric atomic displacements were extracted from the reconstructed phase images using Gaussian fitting of atomic column positions followed by calculation of the relative displacements of these columns for each unit cell (Supplementary Fig. S2). Further details of the analysis are provided in the Methods. To minimize potential artefacts due to crystal tilt, only complex exit waves exhibiting highly symmetric Fourier transforms were employed in the analysis.

Atomic-resolution phase images of GeTe nanocrystals (Fig. 2a,c) provide information transfer beyond 0.7 Å and allow simple discrimination between Ge and Te atomic columns. The high atomic masses of the constituent elements enable the positions of these columns to be determined with an accuracy of a few picometres. Maps of local polar displacements obtained from these reconstructions (Fig. 2b,d) indicate a primarily linear polarization state, albeit with evidence of domain formation in a small fraction of the particles. The polar displacement map illustrated in Fig. 2b, similar to those extracted from the vast majority of reconstructions, illustrates local polar displacements aligned in parallel along a [111]-type direction, consistent with a linear, monodomain polarization state. The local displacements have an average magnitude $\langle\|\mathbf{d}_i\|\rangle$ (where $\mathbf{d}_i$ is the local polar displacement vector of unit cell i) of approximately 0.31 Å with a standard deviation of 0.09 Å, consistent with displacements theoretically predicted for bulk material (~0.35 Å; ref. 30). The magnitude of the overall average polar displacement vector ($\|\langle\mathbf{d}_i\rangle\| = 0.29$ Å) defines the extent of the coherent polar distortion of the entire particle. The ratio $\|\langle\mathbf{d}_i\rangle\|/\langle\|\mathbf{d}_i\|\rangle$ provides a quantitative metric for assessing the degree of linear correlation among local displacement vectors ($\|\langle\mathbf{d}_i\rangle\|/\langle\|\mathbf{d}_i\|\rangle = 0$ indicates no linear correlation, $\|\langle\mathbf{d}_i\rangle\|/\langle\|\mathbf{d}_i\|\rangle = 1$ implies perfect linear correlation). This ratio has a value of approximately 95% for the GeTe nanocrystal in Fig. 2a, indicating strong linear correlation of the local polar displacement vectors. A small portion (<10%) of the polar displacement maps exhibit evidence of more complex, nonlinear patterns. The polar displacement map of Fig. 2d reveals a displacement pattern with two antiparallel polarization domains separated by a (111) plane, consistent with an inversion domain boundary with rotational twinning[31], confirming the ability of this technique to resolve more complex patterns. $\|\langle\mathbf{d}_i\rangle\|$ is reduced considerably (0.04 Å) compared with the value for the particle in Fig. 2a, reflecting the presence of two approximately equal halves with opposing displacement fields.

Phase reconstructions for individual $BaTiO_3$ nanocubes (Fig. 3a,c) provide an atomic-resolution picture of the local

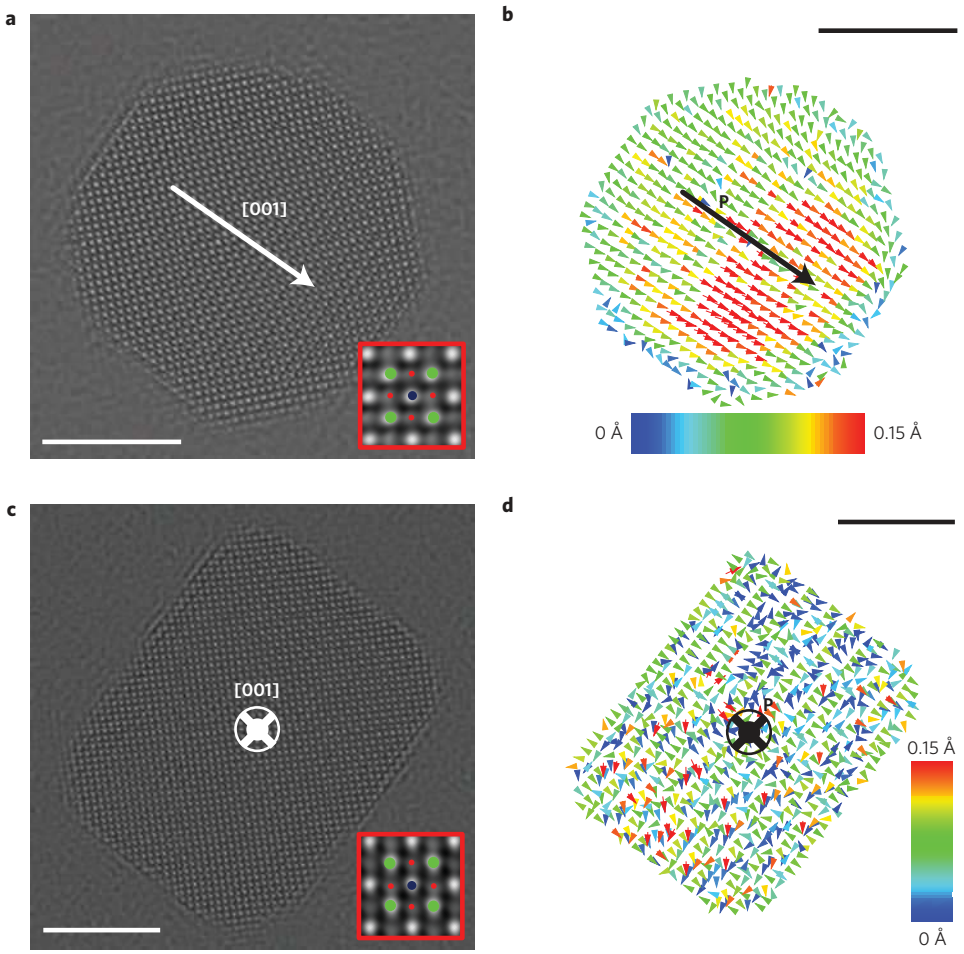

Figure 3 | Atomic-resolution reconstructed phase images and titanium displacement maps of individual $BaTiO_3$ monocrystalline nanocubes. **a**,**b**, Reconstructed phase image of a $BaTiO_3$ nanocube (**a**) and corresponding titanium displacement map (**b**) illustrating a nearly linear, coherent displacement pattern along the [001] axis (scale bars in **a** and **b** are 5 nm, vector magnitudes are given by the colour scale). Inset: magnified view of a $BaTiO_3$ unit cell from the particle demonstrating resolution of Ba (green), Ti/O (blue), and O (red) columns. **c**,**d**, Reconstructed phase image of a $BaTiO_3$ nanocube (**c**) and corresponding titanium displacement map (**d**) illustrating no clear displacement pattern with small displacements, suggesting an out-of-plane polarization orientation (scale bars in **c** and **d** are 5 nm, vector magnitudes are given by the colour scale). Inset: magnified view of a $BaTiO_3$ unit cell from the particle demonstrating resolution of Ba, Ti/O, and O columns. All images were taken along a [100]-type projection.

structure down to an information limit of around 0.7 Å, as for GeTe. All atomic columns, including low-contrast oxygen columns, can be readily distinguished in the images, allowing for precise extraction of the small local titanium displacements that produce the spontaneous polarization. We focus our analysis here on the relative displacements of the Ti/O columns with respect to the Ba sublattice. The direction of the Ti displacement in the unit cell coincides with the direction of the spontaneous polarization in all ferroelectric phases of $BaTiO_3$ and thus provides meaningful insight into the local polarization structure. Titanium displacement maps obtained from these images indicate a primarily linear, monodomain polarization state, as for GeTe, in contrast with theoretical expectations of a toroidal state[11]. The titanium displacement map of Fig. 3b illustrates clear alignment of the Ti displacements for each unit cell along a [001]-type direction, consistent with a ferroelectric tetragonal structure with a linearly ordered polarization. The average magnitude of the local Ti displacements ($\langle\|\mathbf{d}_i\|\rangle = 0.09$ Å with a standard deviation of 0.04 Å) is near the bulk value (~0.09 Å; ref. 25) but smaller than values reported for nanosized $BaTiO_3$ (~0.14 Å), for which local Ti displacement magnitudes can be enhanced relative to bulk material[8,9]. Calculation of the magnitude of the overall average titanium displacement vector $\|\langle\mathbf{d}_i\rangle\|$ yields a value of 0.08(8) Å and a correlation ratio $\|\langle\mathbf{d}_i\rangle\|/\langle\|\mathbf{d}_i\|\rangle$ of ~93%, which indicates clear linear order. The relatively small Ti displacements measured for $BaTiO_3$ compared with the large polar displacements for GeTe are consistent with the larger spontaneous polarization of GeTe (~60 μC cm^{-2} calculated)[12] relative to $BaTiO_3$ (26 μC cm^{-2}; ref. 32), although potential contributions of the oxygen sublattice to the polarization have not been considered in our analysis. No clear pattern is observed in the local Ti displacements presented in Fig. 3d, suggesting a polarization perpendicular to the image plane. The magnitude of the average Ti displacement vector ($\|\langle\mathbf{d}_i\rangle\| = 0.02$ Å) and correlation ratio (~39%) are greatly reduced from those of the particle in Fig. 3b, further supporting this interpretation. The small residual Ti displacement vector calculated for this orientation provides an estimate of the error in the determination of $\|\langle\mathbf{d}_i\rangle\|$ for the particle shown in Fig. 3a. Multislice image simulations for $BaTiO_3$ nanocubes with similar truncated cubic shapes (Supplementary Fig. S3) agree well with experimental reconstructions and indicate a pronounced apparent displacement of the oxygen columns with respect to the Ti/O and Ba columns, even for small tilts (<10 mrad), providing a highly sensitive probe of crystal tilt. The apparent shift of the Ti/O columns, in contrast, is much less pronounced under these tilt conditions. The minimal shift of the oxygen columns at the midpoints between the Ba columns in our experimental phase

images suggests a maximum tilt of less than 10 mrad for these crystals. We note, however, that a small shift of the oxygen sublattice can be observed in Fig. 3c, suggesting a residual tilt of the crystal. The lack of a clear corresponding shift of the Ti/O columns in this image agrees well with our simulation results and indicates that the observed Ti displacement pattern illustrated in Fig. 3b is unlikely to be an artefact of crystal tilt.

Detailed *in situ* studies of individual $BaTiO_3$ nanocubes with nanometre-resolution off-axis electron holography provide further evidence of the linearly ordered, monodomain polarization state and enable direct imaging of the ferroelectric polarization. In off-axis holography, the electron beam from a field emission source is separated into two beams, one passing through the sample and the second passing through vacuum[33]. The overlap of these beams beneath the sample then produces an interference pattern from which the relative phase shift of the sample electron wavefunction can be reconstructed. Electric fields and ferroelectric polarization induce phase shifts of the sample beam with respect to the reference beam from which maps of the local electrostatic potential can be extracted[33,34].

Phase images of $BaTiO_3$ nanocubes suspended over vacuum exhibit a clear electrostatic fringing field, emanating from a [001]-type face at room temperature (Fig. 4a), characteristic of a linear polarization along this axis. On heating the sample above the ferroelectric Curie temperature (130 °C), this field disappears (Fig. 4b), reflecting the non-polar state. *In situ* poling of individual particles with a scanning tunnelling microscope (STM) tip Fig. 4c–e) results in the appearance of a strong, linear polarization along the [001]-type axis perpendicular to the carbon support. Before the application of a bias, the particle exhibits no clear electrostatic fringing field and a flat potential profile in the interior (Fig. 4c,f), suggesting a polarization oriented perpendicular to the image plane. On application of a +3 V bias, a strong fringing field appears parallel to the axis of the STM tip (Fig. 4d), and a strong linear potential gradient can be observed in the particle interior (Fig. 4f), indicating a linear ferroelectric polarization along this axis. The observed phase images are in quantitative agreement with theoretical images obtained from electrostatic calculations (see Methods) for a particle with a linear, monodomain ferroelectric polarization (Supplementary Fig. S4). The absence of a fringing field before the application of a bias discounts charging due to the electron beam as a source for the observed fringing field, and further evidence is provided by the disappearance of the fringing field above the Curie temperature.

Piezoresponse force microscope (PFM) studies provide further evidence for the persistence of a coherent ferroelectric polarization in these particles at room temperature and capture the ultimate stability limit of the ferroelectric state. PFM, a scanned-probe technique that detects local piezoelectric deformations in response to an oscillating electric field[35], has been widely used for nanoscale mapping of ferroelectric domains[36] and local polarization switching[37]. Differences in polarization orientation can be discerned through differences in the phase of the material piezoresponse, with a 180° phase shift with respect to the applied field indicating two antiparallel polarization states[35]. Polarization switching experiments on individual 10 nm $BaTiO_3$ nanocubes illustrate the presence of a clear hysteresis and 180° phase switching at room temperature (Fig. 5a), indicating polarization switching between two antiparallel polarization states. Although the value of the piezoelectric coefficient ($d_{33} = 1.55\,\mathrm{pm\,V^{-1}}$) is significantly reduced from the bulk value ($d_{33} = 75\,\mathrm{pm\,V^{-1}}$; ref. 38), these results are comparable to those obtained for $BaTiO_3$ dots formed through nanosphere lithography with an edge length of 220 nm and a height of 40 nm ($d_{33} = 2\,\mathrm{pm\,V^{-1}}$; ref. 39), which suggests superior preservation of piezoelectric properties for our colloidal nanomaterials. These measurements indicate that stable ferroelectric switching characteristics are clearly maintained at room temperature down to dimensions of less than 10 nm.

Temperature-dependent and size-dependent PFM measurements reveal the ultimate stability limit of the ferroelectric state. The hysteresis loop for 10 nm nanocubes closes at approximately 80 °C (Fig. 5b,c), but a highly nonlinear curve with a 180° phase shift is maintained. PFM measurements of 5 nm nanocubes (Supplementary Fig. S5) demonstrate similar behaviour down to room temperature, with no detectable hysteresis. The sharp transition between polarization states without hysteresis resembles the superparamagnetic state of small magnetic nanoparticles[3], in which aligned local spins undergo collective reorientation under ambient thermal energy, more closely than the paraelectric state of bulk $BaTiO_3$ above the Curie temperature, characterized by a gradual change in polarization with applied field[32]. Our static experiments, however, are unable to distinguish definitively between a conventional paraelectric state and superparaelectric behaviour. Time-resolved measurements will be necessary to determine whether the observed polarization decay is indeed attributable to a dynamic, superparaelectric effect or a consequence of other factors.

The origins of the reduced piezoresponse in our nanocrystals can be elucidated in part through atomic PDF analysis, a powerful X-ray diffraction technique that has been employed for analysis of ferroelectric distortions in nanocrystal ensembles[8–10]. Atomic PDFs were obtained from synchrotron diffraction patterns on 8 and 15 nm $BaTiO_3$ nanocubes, 10 nm $BaTiO_3$ nanospheres, and 8 nm GeTe nanocrystals. The approximate shapes and sizes of these particles are illustrated schematically in Fig. 6d–f. Comparisons of the experimental atomic PDFs for $BaTiO_3$ nanocrystals of all types (Fig. 6a,b and Supplementary Fig. S6) with a tetragonal structural model confirm the presence of local tetragonal distortions at room temperature. The tetragonal distortions maintain local coherence over a length scale of approximately 10 Å for the $BaTiO_3$ nanospheres, with an irregular surface structure, but persist to at least 20 Å for the 8 nm nanocubes and beyond 40 Å for the 15 nm nanocubes. Comparison between atomic PDFs of GeTe (Fig. 6c) with both cubic and rhombohedral structural models indicates the presence of rhombohedral distortions. Calculations of atomic PDFs for 20, 35, and 50 Å length scales (Supplementary Fig. S7) demonstrate the persistence of spatial correlation among these local dipoles to distance scales of ∼5 nm, close to the average particle diameter. These results are in agreement with the TEM measurements indicating a coherent, monodomain polarization state in most GeTe particles.

The significant local structural deviations, particularly for $BaTiO_3$ nanomaterials, observed in our experiments can be attributed to a combination of surface-induced phenomena and depolarization effects. The role of the former is highlighted by comparison of spherical and cubic $BaTiO_3$ nanocrystals of similar size. The very similar geometrical depolarization factors and equivalent material parameters and surface passivation for these samples enable surface phenomena to be examined independently of depolarization effects. A marked decline in the spatial coherence of ferroelectric dipoles can be observed for the spherical sample in our atomic PDF studies, even when compared with cubic particles smaller in size. The cubic particles exhibit nearly atomically flat, low-index surfaces, whereas the spherical particles possess an irregular surface structure with many high-index segments. Internal stresses imposed by free surfaces proportional to $2\gamma/r$—in which γ is the surface energy and r is the particle radius—may approach values of several GPa in sub-10 nm particles[15] and have been found to reduce the magnitude of the cooperative polar distortion in nanosized perovskites[40]. The preponderance of high-energy surface facets and irregular surface structure of the spherical particles probably enhance both the overall internal stresses and the inhomogeneity of the strain field, resulting in a reduction of

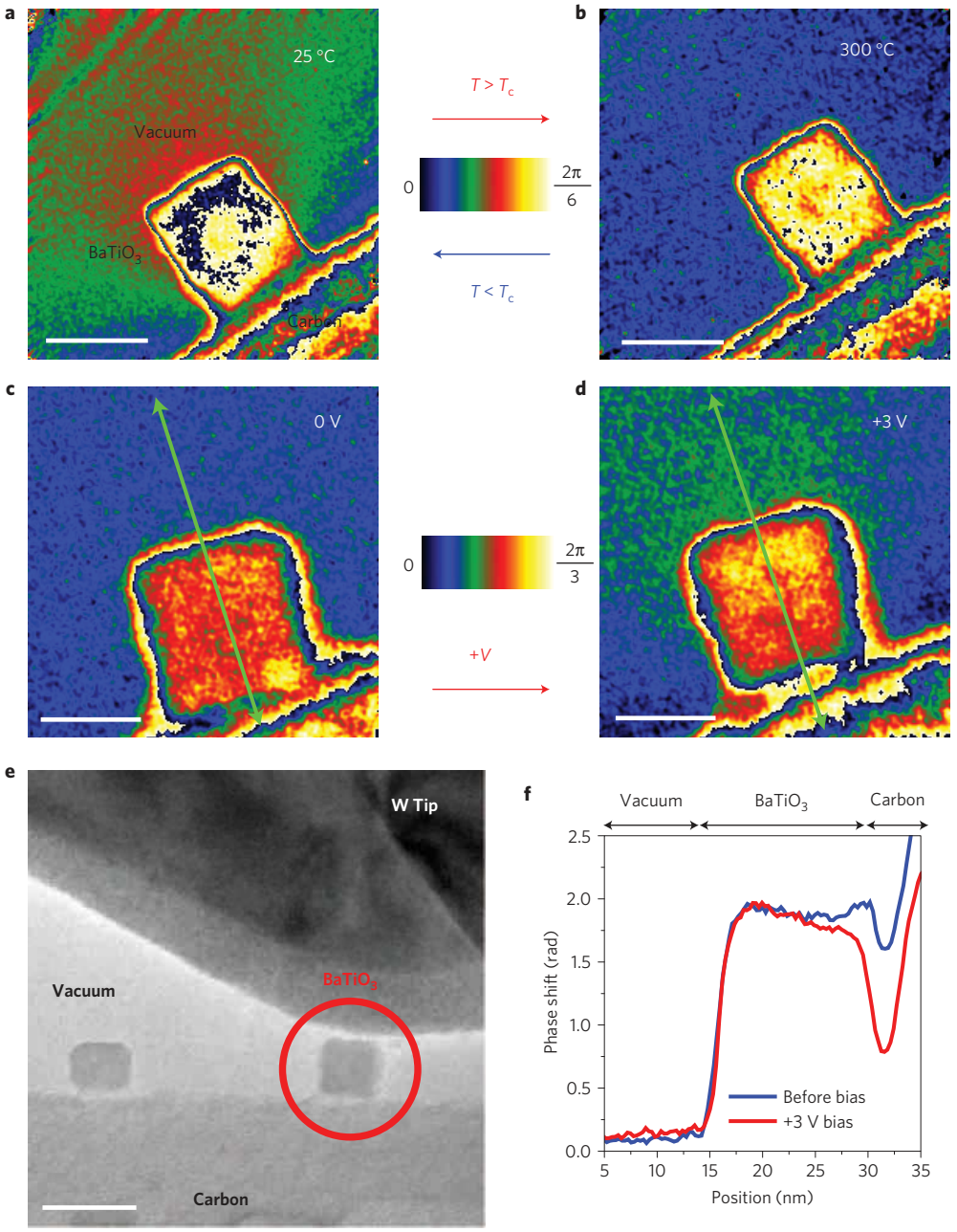

Figure 4 | Direct polarization imaging of individual $BaTiO_3$ nanocubes with off-axis electron holography. a,**b**, Phase images of an individual $BaTiO_3$ nanocube above (**b**) and below (**a**) the ferroelectric Curie temperature (130 °C) illustrating a fringing field emanating from the [001] face that disappears above T_c (scale bars, 10 nm). **c**,**d**, Reconstructed phase images of a second individual $BaTiO_3$ nanocube before application of an electrical bias (**c**) and after application of a +3 V bias (**d**, scale bars, 10 nm). No fringing field can be observed before application of a bias; clear fringing fields emanating from the [001] face can be observed after electrical poling. **e**, TEM image of the integrated STM tip nearing contact with the individual $BaTiO_3$ cube imaged in panels **c** and **d** (scale bar, 25 nm). **f**, Corresponding line profiles for **c** and **d** (green arrows) demonstrating the appearance of a strong linear phase gradient on electrical poling. All phase images have been amplified for clarity (six times for **a** and **b**, three times for **c** and **d**).

the cooperative polar distortion and an enhancement of structural disorder, leading to the observed reduction in spatial coherence. It is notable that cubic particles smaller in size (but with a greater surface area and surface-to-volume ratio) retain markedly stronger spatial dipole correlations. The surface effect here is thus not simply a function of surface-to-volume ratio, but rather a more complex effect governed by the specific energies and arrangements of surface facets. These results indicate that careful control over surface terminations and particle shape control, a key advantage of colloidal synthetic procedures, may provide a pathway to the stabilization of ferroelectric order in nanoscale crystals.

Insight into the influence of depolarization effects may be obtained from the comparison of highly conducting GeTe with strongly insulating $BaTiO_3$ nanocrystals of comparable sizes and shapes. The large free carrier density ($\sim 10^{21}$ cm^{-3}) of GeTe is expected to provide metallic conduction and strong internal screening of the polarization, minimizing depolarization effects. PDF analysis indicates markedly enhanced spatial correlations in GeTe (correlation length of ~5 nm for 8 nm particles) relative to $BaTiO_3$ (correlation length of ~2 nm for 8 nm nanocubes), although the correlation range does not span the entire diameter of the particles. These observations suggest a strong stabilization of

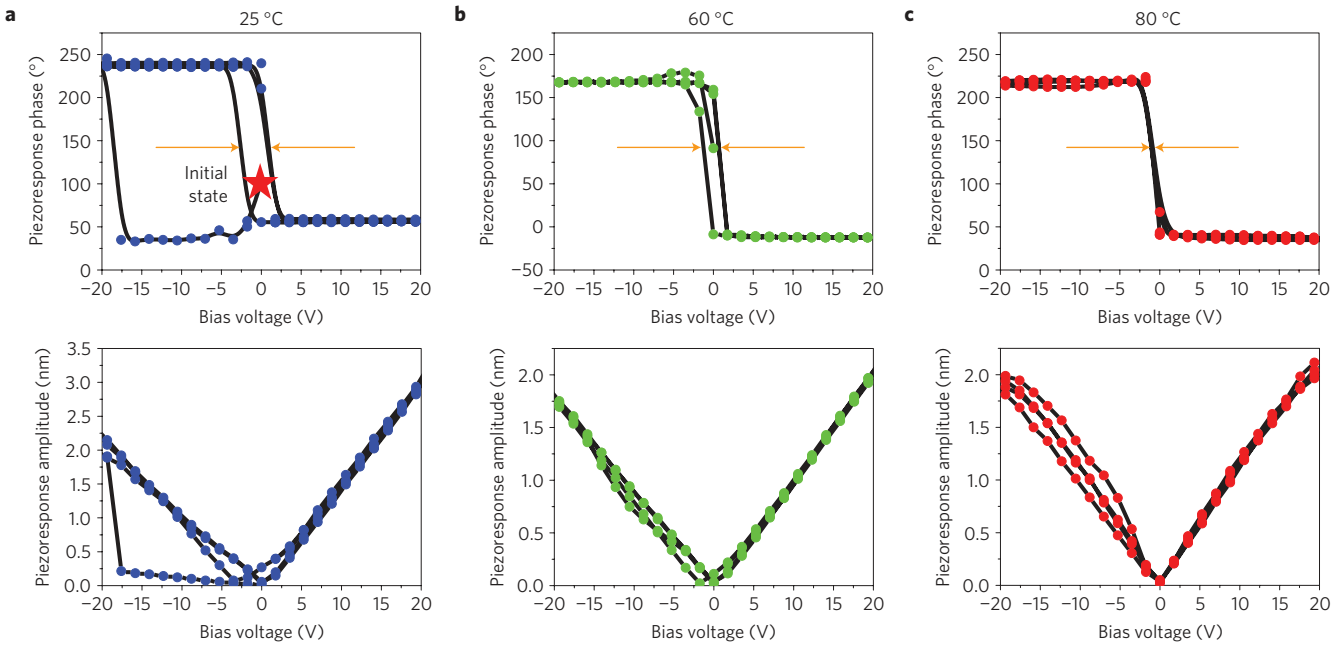

Figure 5 | Temperature-dependent PFM measurements of individual $BaTiO_3$ nanocubes. a, Piezoresponse phase (top) and amplitude (bottom) for a single 10 nm $BaTiO_3$ nanocube at room temperature. A clear hysteresis and 180° phase switching can be observed. **b**, Piezoresponse phase (top) and amplitude (bottom) for the same 10 nm $BaTiO_3$ nanocube at 60 °C. A markedly decreased hysteresis is observed. **c**, Piezoresponse phase (top) and amplitude (bottom) for the same 10 nm $BaTiO_3$ nanocube at 80 °C. Although sharp 180° phase switching is maintained, the hysteresis collapses.

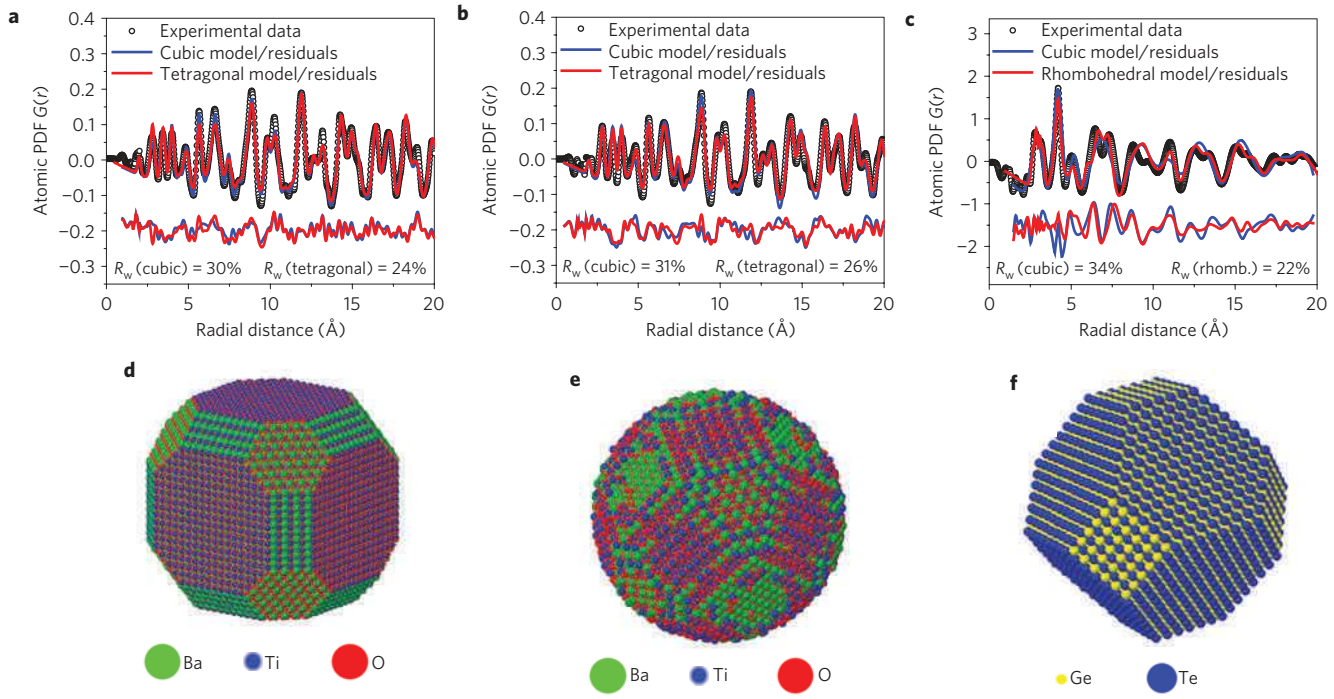

Figure 6 | Atomic PDF analysis of GeTe and $BaTiO_3$ nanocrystal ensembles. a,**b**, Atomic PDFs for 8 nm $BaTiO_3$ nanocubes (**a**) and 10 nm $BaTiO_3$ nanospheres (**b**) compared with cubic (blue, top) and tetragonal (red, top) structural models. Residual curves for both the cubic (blue) and tetragonal (red) structural models are shown at the bottoms of the plots. **c**, Atomic PDF for 8 nm GeTe nanocrystals compared with cubic (blue, top) and rhombohedral (red, top) structural models. Residual curves for both the cubic (blue) and rhombohedral (red) structural models are shown at the bottom of the plot. **d**–**f**, Model structures for 8 nm $BaTiO_3$ nanocubes (**d**), 10 nm $BaTiO_3$ nanospheres (**e**), and 8 nm GeTe nanocrystals (**f**). The model PDFs featuring cooperative polar distortions (tetragonal for $BaTiO_3$ and rhombohedral for GeTe) yield a superior though imperfect match to the experimental data.

the linearly ordered polar state in GeTe by internal carriers. Both the PDF analysis and TEM studies, however, indicate considerable structural disorder and inhomogeneity in the polarization patterns of GeTe nanomaterials, suggesting a strong surface contribution. Previous work[41] indicated a decline in the overall rhombohedral lattice distortion with decreasing particle size, further supporting this interpretation. It is clear from these experiments that both surface structure and depolarization effects exercise a profound

influence on the stability and nature of the polar state in low-dimensional nanosystems. Minimizing the contributions of both mechanisms sets an ultimate limit for the size-scaling of the polar-ordered phase. The highly conductive GeTe nanocrystals employed in this experiment, with atomically flat, well-passivated, and low-index surface facets and maximal compensation of depolarization effects, provide nearly ideal conditions for the preservation of ferroelectric order at finite dimensions. The dissolution of spatial correlations among local ferroelectric dipoles beyond ~5 nm in our 8 nm GeTe nanocrystals thus suggests an ultimate, intrinsic lower bound for the existence of cooperative ferroelectric order in nanomaterials. Previous literature has indicated a decay of the spontaneous polarization in the vicinity of a free surface over a distance scale known as the extrapolation length[13,26]. The correlation range of ferroelectric dipoles measured in our experiments (~5 nm) relative to the particle diameter (~8 nm) is consistent with a coherent, linearly ordered polarization state with reduced polarization in an exterior shell with a thickness of ~1.5 nm, in strong agreement with typical extrapolation lengths measured experimentally[26]. The stability of the polar state under near-perfect screening conditions is thus ultimately restricted to a length scale of approximately 3 nm, although reduction of the spontaneous polarization throughout the particle volume via surface-induced internal pressure will probably further limit the experimentally achievable stability range of the polar state. This result is consistent with theoretical predictions[11] of an ultimate size limit of 2.6 nm for the preservation of (toroidal) ferroelectric correlations in ideal perovskite nanodots.

The decline in dipole correlations in $BaTiO_3$ nanocrystals of all types relative to GeTe suggests incomplete screening of polarization-induced surface charges in the former material, leading to depolarization fields. Although molecular adsorbates probably provide partial screening, consistent with previous work on micrometres-long $BaTiO_3$ nanowires[42], the observation of electrostatic fringing fields in our holography experiments is strongly suggestive of incomplete screening of these polarization-induced charges. This interpretation is in strong agreement with observations indicating a $1/d_{nw}$ scaling relationship between the Curie temperature and the nanowire diameter, d_{nw}, attributed to incomplete compensation of polarization charges[42]. The stability of a linear polarization state under incomplete screening conditions contrasts with theoretical reports predicting a toroidal state for all screening conditions with the exception of nearly perfect short-circuit boundary conditions[43]. Despite imperfect screening conditions, the classical nearly linear, monodomain polarization state remains surprisingly stable, persisting at room temperature down to particle sizes of less than 10 nm. These findings also contrast with previous experimental studies of local polarization patterns in thin-film samples indicating flux-closure, in some cases through continuous rotation of local polarization vectors[27,44]. Flux-closure in these structures is facilitated by the growth of thin ferroelectric layers on highly insulating substrates, such as $SrTiO_3$ and $TbScO_3$, leading to substantial polarization charges at the film–substrate interfaces. Transferring these results to free-standing nanostructures may provide a promising pathway towards stabilizing novel polarization patterns in these materials. Replacing molecular adsorbates bound to the surfaces of the ferroelectric core with an epitaxial shell layer of an inorganic, insulating oxide, such as $SrTiO_3$ on $BaTiO_3$, may inhibit polarization charge screening and enable experimental realization of true monodomain toroidal polarization states.

It is also notable that the polarization generally exists in a monodomain state. Several recent works on ion-milled single crystals of $BaTiO_3$ have demonstrated the formation of complex domain states, including flux-closure arrangements, down to the smallest dimensions accessible in these experiments (~100 nm; refs 45,46). The rich domain structures examined in these experiments, with periodicities generally consistent with the classic domain scaling laws first described by Kittel, contrast with the monodomain polarization states observed here. Our experiments thus suggest that these scaling laws, valid over more than six orders of magnitude in size, ultimately break down at nanometre length scales, consistent with a previous study demonstrating a transition to a multidomain state at particle sizes of ~30 nm (ref. 18). It should be noted, however, that the distinction between monodomain and multidomain states may be a more complex function of both size effects and surface conditions. A previous study of nanomilled samples, for example, pointed to internal strains imposed by surface tension as a driving force for an additional ferroelastic contribution to domain formation in free-standing samples[47]. The pronounced differences in surface structure between our materials and nanomilled samples exhibiting complex domain structures may thus also contribute to this contrast in experimental results.

This work provides atomic-scale insight into the fundamental nature of ferroelectric order down to its ultimate size limit. Atomic-resolution mapping of local ferroelectric distortions indicates a coherent, nearly linear, monodomain state accompanied by local structural distortions. The persistence of ferroelectric coherence in $BaTiO_3$ is further supported by single-particle studies with off-axis electron holography and PFM measurements of individual nanocubes demonstrating ferroelectric switching behaviour at room temperature. These PFM studies further demonstrate the ultimate stability limit of ferroelectric order. Careful atomic PDF studies point to the parallel roles played by surface-induced relaxation and depolarization effects in the dissolution of ferroelectric order at finite dimensions and indicate considerable structural disorder and dipole decoherence, even in conductive GeTe with strong polarization screening. These studies also demonstrate the utility of colloidal morphology control as a means of stabilizing the polar state at nanoscale dimensions. These experiments reveal the ultimate limit of the ferroelectric state and provide a pathway to unravelling the fundamental physics of nanoscale ferroelectricity at the smallest possible size scales.

Methods

Synthesis of GeTe and $BaTiO_3$ nanomaterials. GeTe nanocrystals were prepared following a previous literature report[18]. In a typical synthesis, a flask containing 0.1 g of Ge(II) bis–bis(trimethylsilyl)amide dissolved in 6 ml of squalane and 1 ml of trioctylphosphine (TOP) was heated to 230 °C under argon. 1 ml of a 10 wt% solution of Te in TOP mixed with an additional 0.5 ml of TOP and 0.03 g of 1-dodecanethiol was injected into the flask. The reaction mixture was then held at 220 °C for 1–2 min. $BaTiO_3$ nanocubes were prepared following ref. 17. In a typical synthesis, a Teflon-lined autoclave vessel (Parr Instruments) was loaded with solutions of $Ba(NO_3)_2$ (1 mmol) in 5 ml of deionized water, NaOH (12.5 mmol) in 5 ml of deionized water, Ti(IV) *n*-butoxide (1 mmol) in 5 ml of 1-butanol, 2.5 ml of oleic acid, and 5 ml of 1-butanol and heated to 135 °C for 18 h. To prepare quasi-spherical $BaTiO_3$ particles, the reaction temperature was held at 150 °C for 24 h, and the molar ratio between water and 1-butanol was decreased.

Atomic-resolution TEM. Atomic-resolution high-resolution TEM image series of $BaTiO_3$ and GeTe nanocrystals were acquired using the TEAM 1 microscope at the National Center for Electron Microscopy, a modified FEI Titan 80-300 equipped with a combined spherical and chromatic aberration corrector on the imaging side, a special high-brightness field emission gun, and a Gatan Image Filter. Through-focus series consisting of 30 images were taken at defocus values ranging from 300 to −300 Å with a negative coefficient of spherical aberration of approximately −15 µm. $BaTiO_3$ images were acquired at an accelerating voltage of 300 kV, and GeTe images were acquired at 80 kV. All samples were imaged on ultrathin carbon grids from Ted Pella. The electron wavefunction at the exit plane of the specimen was reconstructed using the Gerchberg–Saxton algorithm implemented in MacTempas X by Total Resolution. The resulting phase images were Fourier filtered using the background subtraction filter feature in MacTempas; this filtering did not alter the observed displacement patterns. Atomic column positions were extracted using the peak finding and Gaussian fitting routines of MacTempas. Polar displacement maps were constructed from the fit peak positions using custom Matlab code, which groups these peak positions into unit cells and calculates the displacement between the centre points of Ge and Te atomic columns for GeTe or the displacements of the Ti/O columns

with respect to the Ba columns of each unit cell for $BaTiO_3$. Source code is available on request.

Off-axis electron holographic imaging of $BaTiO_3$ nanocubes. Holographic images of individual $BaTiO_3$ nanocubes were acquired using a JEOL 3000F TEM at Brookhaven National Laboratory operated at 300 kV equipped with a field emission gun, Gatan Image Filter, Lorentz lens, and biprism. Holograms were acquired with a biprism voltage of 50 V, and reference images were taken over vacuum. Holograms were taken of particles suspended over vacuum on the edge of a lacey carbon grid. Phase images were reconstructed using custom Gatan Digital Micrograph scripts; source code is available on request. Nanocubes were heated above the Curie point using a Gatan heating holder, and individual nanocubes were poled using a Nanofactory probe holder with an integrated tungsten STM tip. To enable access to particles on the carbon grid for the poling experiments, the copper/carbon grid was cut in half, leaving several copper grid squares exposed. The phase profiles presented in Fig. 4f were calculated in Gatan Digital Micrograph using the line profile tool.

Simulated phase images for $BaTiO_3$ nanocubes were numerically calculated on the basis of the phase shift of the electron wave due to the variation of the projected electrostatic potential or field. The spontaneous polarization charge (P_S) on one side of a $BaTiO_3$ nanocube was treated as a square sheet charge with uniform charge density P_S. For a square with a side length of $2a$ and a uniform surface charge P_S, the centre of which is the origin, the potential $V(x,y,z)$ can be obtained by summing the contributions of elementary charges $P_S dx' dz'$:

$$V(x,y,z) = \frac{P_S}{4\pi\varepsilon_o\varepsilon_r}\int_{-a}^{a}\int_{-a}^{a}\frac{dx'dz'}{\sqrt{(x-x')^2+y^2+(z-z')^2}} = \frac{P_S}{4\pi\varepsilon_o\varepsilon_r}\int_{-a}^{a}\ln\left[\frac{a+x+\sqrt{(x+a)+y^2+(z-z')^2}}{-a+x+\sqrt{(x-a)^2+y^2+(z-z')^2}}\right]dz'$$

In this equation, ε_0 represents the permittivity of free space and ε_r the dielectric constant. The electron wave passing near the nanocube will be perturbed by the above potential fields along the beam path (z-axis) and give rise to a corresponding phase image ($\Delta\varphi(x,y)$) according to the following equation:

$$\Delta\varphi(x,y) = C_E\int_{-\infty}^{\infty}V(x,y,z)dz = \frac{C_E P_S}{4\pi\varepsilon_o\varepsilon_r}\int_{-\infty}^{\infty}\int_{-a}^{a}\ln\left[\frac{a+x+\sqrt{(x+a)+y^2+(z-z')^2}}{-a+x+\sqrt{(x-a)^2+y^2+(z-z')^2}}\right]dz'dz$$

Here, C_E is an energy-related constant with a value of 6.526 mrad V^{-1} nm^{-1} for 300 keV electrons. The above double-integration problem was solved numerically using a Gatan Digital Micrograph script to generate the simulated phase images. In addition, to address the contact of the $BaTiO_3$ nanocube with the conducting carbon grid, a mirror square charge was set up to ensure zero potential on the carbon surface. This manipulation is equivalent to complete compensation of the spontaneous polarization charge on the side of the $BaTiO_3$ nanocube in contact with the carbon grid. Inside the $BaTiO_3$ nanocube, the mean inner-potential experienced by incident electrons yields a constant phase shift. A value of 17.9 V was extracted from the phase profile to fit the experimental data. Quantitative agreement with experimental phase images was achieved for $\varepsilon_r = 60$.

Piezoresponse force measurements of individual $BaTiO_3$ nanocubes. The polarization switching and local piezoelectric response of $BaTiO_3$ nanocrystals were studied at room temperature with an Asylum Research MFP-3D atomic force microscope working in contact mode. An AC240TM cantilever made of a tetrahedral silicon tip coated with platinum/titanium was used to apply a small a.c. voltage with an amplitude of 40 mV. Measurements were performed by applying two oscillating voltages with frequencies below and above resonance (270 kHz), operating the cantilever in the dual a.c. resonance tracking mode[48]. The piezoresponse of the nanocubes was detected as the first-harmonic component of the deflection of the tip, $d = d_0 + A\cos(\omega t + \varphi)$, where φ is the phase of the piezoelectric signal, d_0 is an initial deflection, A the amplitude, t the time, and ω the frequency. The photodetector signal amplitude was demodulated with a lock-in amplifier and the values of the piezoelectric coefficient were obtained after calibrating the photodetector signal.

Atomic PDF analysis of $BaTiO_3$ and GeTe nanocrystals. X-ray diffraction (XRD) measurements were carried out at beamline 11-ID-C at the Advanced Photon Source at Argonne National Laboratory using X-rays with an energy of 115.232 keV ($\lambda = 0.1076$ Å) and a large-area detector. Several scans were taken and averaged to improve the XRD data statistics. The XRD data were reduced to atomic PDF ($G(r)$) using the program RAD (ref. 49). The atomic PDFs were fit with structure models featuring long-range ordered dipoles and no dipoles. The fits were completed with the help of the program PDFgui[50].

Received 2 December 2011; accepted 29 May 2012; published online 8 July 2012

References

1. Bawendi, M. G., Steigerwald, M. L. & Brus, L. E. The quantum mechanics of larger semiconductor clusters (quantum dots). *Annu. Rev. Phys. Chem.* **41,** 477–496 (1990).
2. Law, M., Goldberger, J. & Yang, P. Semiconductor nanowires and nanotubes. *Annu. Rev. Mater. Sci.* **34,** 83–122 (2004).
3. Murray, C. B. *et al.* Colloidal synthesis of nanocrystals and nanocrystal superlattices. *IBM J. Res. Dev.* **45,** 47–56 (2001).
4. Scott, J. F. Applications of modern ferroelectrics. *Science* **315,** 954–959 (2007).
5. Scott, J. F. & Paz de Araujo, C. A. Ferroelectric memories. *Science* **246,** 1400–1405 (1989).
6. Chattopadhyay, S., Ayyub, P., Palkar, V. R. & Multani, M. Size-induced diffuse phase transition in the nanocrystalline ferroelectric $PbTiO_3$. *Phys. Rev. B* **52,** 13177–13183 (1995).
7. Zhong, W. L., Wang, Y. G., Zhang, P. L. & Qu, B. D. Phenomenological study of the size effect on phase transitions in ferroelectric particles. *Phys. Rev. B* **50,** 698–703 (1994).
8. Smith, M. B. *et al.* Crystal structure and the paraelectric-to-ferroelectric phase transition of nanoscale $BaTiO_3$. *J. Am. Chem. Soc.* **130,** 6955–6963 (2008).
9. Petkov, V., Gateshki, M., Niederberger, M. & Ren, Y. Atomic-scale structure of nanocrystalline $Ba_xSr_{1-x}TiO_3$ ($x = 1$, 0.5, 0) by X-ray diffraction and the atomic pair distribution function technique. *Chem. Mater.* **18,** 814–821 (2006).
10. Page, K., Proffen, T., Niederberger, M. & Seshadri, R. Probing local dipoles and ligand structure in $BaTiO_3$ nanoparticles. *Chem. Mater.* **22,** 4386–4391 (2010).
11. Naumov, I. I., Bellaiche, L. & Fu, H. Unusual phase transitions in ferroelectric nanodisks and nanorods. *Nature* **432,** 737–740 (2004).
12. Durgun, E., Ghosez, P., Shaltaf, R., Gonze, X. & Raty, J-Y. Polarization vortices in germanium telluride nanoplatelets: A theoretical study. *Phys. Rev. Lett.* **103,** 247601 (2009).
13. Kretschmer, R. & Binder, K. Surface effects on phase transitions in ferroelectrics and dipolar magnets. *Phys. Rev. B* **20,** 1065–1076 (1979).
14. Batra, I. P., Wurfel, P. & Silverman, B. D. New type of first-order phase transition in ferroelectric thin films. *Phys. Rev. Lett.* **30,** 384–387 (1973).
15. Morozovska, A. N., Glinchuk, M. D. & Eliseev, E. A. Phase transitions induced by confinement of ferroic nanoparticles. *Phys. Rev. B* **76,** 014102 (2007).
16. Urban, J. J., Yun, W. S. & Park, H. Synthesis of single-crystalline perovskite nanorods composed of barium titanate and strontium titanate. *J. Am. Chem. Soc.* **124,** 1186–1187 (2002).
17. Adireddy, S., Lin, C., Cao, B., Zhou, W. & Caruntu, G. Solution-based growth of monodisperse cube-like $BaTiO_3$ colloidal nanocrystals. *Chem Mater.* **22,** 1946–1948 (2010).
18. Polking, M. J., Zheng, H., Ramesh, R. & Alivisatos, A. P. Controlled synthesis and size-dependent polarization domain structure of colloidal germanium telluride nanocrystals. *J. Am. Chem. Soc.* **133,** 2044–2047 (2011).
19. Chopra, K. L. & Bahl, S. K. Amorphous and crystalline GeTe films. I. Growth and structural behavior. *J. Appl. Phys.* **40,** 4171–4178 (1969).
20. Steigmeier, E. F. & Harbeke, G. Soft phonon mode and ferroelectricity in GeTe. *Solid State Commun.* **8,** 1275–1279 (1970).
21. Bahl, S. K. & Chopra, K. L. Amorphous versus crystalline GeTe films. II. Optical properties. *J. Appl. Phys.* **40,** 4940–4947 (1969).
22. Chattopadhyay, T., Boucherle, J. X. & Von Schnering, H. G. Neutron diffraction study on the structural phase transition in GeTe. *J. Phys. C* **20,** 1431–1440 (1987).
23. Edwards, A. H. *et al.* Electronic structure of intrinsic defects in crystalline germanium telluride. *Phys. Rev. B* **73,** 045210 (2006).
24. Lines, M. E. & Glass, A. M. *Principles and Applications of Ferroelectrics and Related Materials* (Clarendon, 1977).
25. Kwei, G. H., Lawson, A. C., Billinge, S. J. L. & Cheong, S-W. Structures of the ferroelectric phases of barium titanate. *J. Phys. Chem.* **97,** 2368–2377 (1993).
26. Jia, C-L. *et al.* Unit-cell scale mapping of ferroelectricity and tetragonality in epitaxial ultrathin ferroelectric films. *Nature Mater.* **6,** 64–69 (2007).
27. Jia, C-L., Urban, K.W., Alexe, M., Hesse, D. & Vrejoiu, I. Direct observation of continuous electric dipole rotation in flux-closure domains in ferroelectric $Pb(Zr,Ti)O_3$. *Science* **331,** 1420–1423 (2011).
28. Gerchberg, R. W. & Saxton, W. O. A practical algorithm for the determination of the phase from image and diffraction plane pictures. *Optik* **35,** 237–246 (1972).
29. Coene, W., Janssen, G., Op de Beeck, M. & Van Dyck, D. Phase retrieval through focus variation for ultra-resolution in field-emission transmission electron microscopy. *Phys. Rev. Lett.* **69,** 3743–3746 (1992).
30. Lencer, D. *et al.* A map for phase-change materials. *Nature Mater.* **7,** 972–977 (2008).
31. Snykers, M., Delavignette, P. & Amelinckx, S. The domain structure of GeTe as observed by electron microscopy. *Mater. Res. Bull.* **7,** 831–839 (1972).
32. Merz, W. J. Double hysteresis loop of $BaTiO_3$ at the Curie point. *Phys. Rev.* **91,** 513–517 (1953).

33. McCartney, M. R. & Smith, D. J. Electron holography: Phase imaging with nanometer resolution. *Annu. Rev. Mater. Sci.* **37,** 729–767 (2007).
34. Lichte, H., Reibold, M., Brand, K. & Lehmann, M. Ferroelectric electron holography. *Ultramicroscopy* **93,** 199–212 (2002).
35. Kalinin, S. V. & Bonnell, D. A. Imaging mechanism of piezoresponse force microscopy of ferroelectric surfaces. *Phys. Rev. B* **65,** 125408 (2002).
36. Nagarajan, V. *et al.* Dynamics of ferroelastic domains in ferroelectric thin films. *Nature Mater.* **2,** 43–47 (2003).
37. Maksymovych, P. *et al.* Polarization control of electron tunneling into ferroelectric surfaces. *Science* **324,** 1421–1425 (2009).
38. Jona, F. & Shirane, G. *Ferroelectric Crystals* (Dover, 1993).
39. Ma, W. & Hesse, D. Microstructure and piezoelectric properties of sub-80 nm high polycrystalline $SrBi_2Ta_2O_9$ nanostructures within well-ordered arrays. *Appl. Phys. Lett.* **85,** 3214–3216 (2004).
40. Shiratori, Y., Pithan, C., Dornseiffer, J. & Waser, R. Raman scattering studies on nanocrystalline $BaTiO_3$ part I—isolated particles and aggregates. *J. Raman Spectros.* **38,** 1288–1299 (2007).
41. Polking, M. J. *et al.* Size-dependent polar ordering in colloidal GeTe nanocrystals. *Nano Lett.* **11,** 1147–1152 (2011).
42. Spanier, J. E. *et al.* Ferroelectric phase transition in individual single-crystalline $BaTiO_3$ nanowires. *Nano Lett.* **6,** 735–739 (2006).
43. Ponomareva, I., Naumov, I. I. & Bellaiche, L. Low-dimensional ferroelectrics under different electrical and mechanical boundary conditions: Atomistic simulations. *Phys. Rev. B* **72,** 214118 (2005).
44. Nelson, C. T. *et al.* Spontaneous vortex nanodomain arrays at ferroelectric heterointerfaces. *Nano Lett.* **11,** 828–834 (2011).
45. Schilling, A. *et al.* Domains in ferroelectric nanodots. *Nano Lett.* **9,** 3359–3364 (2009).
46. McQuaid, R. G. P., McGilly, L. J., Sharma, P., Gruverman, A. & Gregg, J. M. Mesoscale flux-closure domain formation in single-crystal $BaTiO_3$. *Nature Commun.* **2,** 404 (2011).
47. Luk'yanchuk, I. A., Schilling, A., Gregg, J. M., Catalan, G. & Scott, J. F. Origin of ferroelastic domains in free-standing single-crystal ferroelectric films. *Phys. Rev. B* **79,** 144111 (2009).
48. Rodriguez, B. J., Callahan, C., Kalinin, S. V. & Proksch, R. Dual-frequency resonance-tracking atomic force microscopy. *Nanotechnology* **18,** 475504 (2007).
49. Petkov, V. RAD, a program for analysis of X-ray diffraction data from amorphous materials for personal computers. *J. Appl. Crystallogr.* **22,** 387–389 (1989).
50. Farrow, C. L. *et al.* PDFfit2 and PDFgui: Computer programs for studying nanostructure in crystals. *J. Phys. Condens. Matter* **19,** 335219 (2007).

Acknowledgements

The authors would like to thank Shiva Adireddy for the synthesis of the $BaTiO_3$ nanomaterials used in this manuscript; P. Ercius, T. Duden, Y. Ren and A. Gautam for technical assistance and helpful discussions; and H. Park for critical feedback on the manuscript. In addition, the authors gratefully acknowledge M. R. McCartney for providing scripts for the analysis of the holographic images. Access to the electron microscopy facility at the Center for Functional Nanomaterials, Brookhaven National Laboratory, is acknowledged. Work at the National Center for Electron Microscopy was supported by the US Department of Energy, Division of Materials Sciences and Division of Chemical Sciences, under contract no. DE-AC02-05CH11231. Electron holography experiments at Brookhaven National Laboratory were supported by the US Department of Energy, Division of Materials Sciences and Division of Chemical Sciences, under contract no. DE-AC02-98CH10886 and were carried out in part at the Center for Functional Nanomaterials, Brookhaven National Laboratory. Synchrotron X-ray diffraction measurements at the Advanced Photon Source were supported by the Office of Science, Office of Basic Energy Sciences, of the US Department of Energy under Contract DE-AC02-06CH11357. Work on piezoresponse force measurements and synthesis of $BaTiO_3$ nanostructures was supported by the National Science Foundation through grants no. NSF-MSN CAREER-1157300, no. EPS-1003897 and no. NSF-DMR-1004869. All other work was supported by the Physical Chemistry of Nanocrystals Project of the Director, Office of Science, Office of Basic Energy Sciences, Materials Sciences and Engineering Division, of the US Department of Energy under contract no. DE-AC02-05CH11231. M.J.P. was supported by a National Science Foundation Graduate Research Fellowship and by a National Science Foundation Integrative Graduate Education and Research Traineeship fellowship.

Author contributions

M.J.P. conceived the experiment, performed atomic-resolution TEM studies of GeTe and $BaTiO_3$ nanocrystals and analysed the results, participated in holographic imaging experiments with M-G.H. and Y.Z., interpreted data, and wrote the manuscript. A.Y. acquired piezoresponse force data on $BaTiO_3$ nanocubes under the supervision of G.C. Analysis of the PFM data was performed by G.C. and A.Y. V.P. acquired atomic PDF data and analysed the results, and C.F.K. assisted in the analysis of the TEM data. V.V.V performed phase image simulations for the holographic images. R.R. and A.P.A. supervised the work and provided critical feedback on the manuscript.

Additional information

The authors declare no competing financial interests. Supplementary information accompanies this paper on www.nature.com/naturematerials. Reprints and permissions information is available online at www.nature.com/reprints. Correspondence and requests for materials should be addressed to A.P.A. or R.R.